



Plasmonic metasensor for simultaneous detection of relative humidity and temperature in terahertz band

QianRu Ma, Yi Ma, ZeShuai Ren, Lin Chen*

Shanghai Key Lab of Modern Optical System, University of Shanghai for Science and Technology, Shanghai, 200093, People's Republic of China

ARTICLE INFO

Keywords:

Plasmonic metasensor
Terahertz
Electromagnetic induced transparency
Humidity
Temperature

ABSTRACT

A terahertz plasmonic metasensor is demonstrated for simultaneous measurement of relative humidity (RH) and temperature at the first time. Double golden rings can excite electromagnetic induced transparency (EIT) with dual plasmonic resonances. By studying the relationship between resonance frequencies at both resonance dips and environmental parameters, the RH sensitivities are 0.14 GHz/% (−282 nm/%) at low frequency (dip A) and 0.27 GHz/% (−210 nm/%) at high frequency (dip C), while the temperature sensitivities are 1.35 GHz/°C (−2718 nm/°C) at dip A and 2.45 GHz/°C (−1906 nm/°C) at dip C. Additionally, the influences of temperature and RH are proven independent on frequency shifts, indicating a suitability with RH and temperature changes simultaneously. The proposed metasensor covers advantages of polarization-incident insensitivity, high sensitivity, easy integration and low cost, making wide applications in industrial manufacturing, clinical medicine, weather forecasting and human health.

1. Introduction

Temperature and relative humidity (RH) are crucial parameters applied in food industry [1], human comfort [2] and clinical situation [3]. Decent temperature and RH can ensure quality food products and longer storage time, comfortable environment, as well as suitable diagnostic conditions. For medical diagnosis, a wearable fiber Bragg grating (FBG) humidity sensor encapsulated in silicone rubber was proposed for the monitoring of respiratory and cardiac rate, in which the sensing performance to humidity and temperature response was experimentally assessed [4]. Owing to specific application scenarios, a wide variety of humidity sensing technologies have been developed, including optical [5–7], capacitive/resistive [8,9] and electrochemical [10]. Compared with capacitive/resistive humidity sensors that are more susceptible to electromagnetic interference and corrosion in electrochemical humidity sensors, optical humidity sensors show many advantages such as fast response, high sensitivity, electromagnetic immunity and durability in extreme environment [11].

Conventional micro-nano optical sensors enhance the localized optical field intensity by means of light diffraction and refraction effects, micro-resonant cavity cavities and optical interferometers to improve the detection sensitivity. They are capable of simultaneous measurement of humidity and temperature, including FBG [12], Fabry–Perot

interferometer (FPI) [13], Mach–Zehnder interferometer [14], optical fiber [15]. Liu et al. [12] printed polymer microbeams at the end of single-mode fiber to achieve a humidity sensitivity of 0.348 nm/% (between 40% and 90% humidity at a temperature of 25 °C ± 0.1 °C) and a temperature sensitivity of −0.356 nm/°C (40% ± 1% humidity between 25 °C and 70 °C). This work innovatively proposed to combine FBG with FPI using femtosecond laser-induced two-photon polymerization to print the polymer microcantilever at the end of a single-mode fiber. Hydrophilic materials are keys to humidity sensing properties, like polyacrylic acid [16], silicon dioxide [17], titanium oxide [18] and polyvinyl alcohol (PVA) [19–21]. Among these materials, PVA is a remarkable choice as its extraordinary hygroscopicity, stability, flexibility and low cost. In 2022, Li et al. [21] proposed a dual C-shaped FPI fiber filled with polydimethylsiloxane (PDMS) and PVA, in which PDMS is sensitive to temperature and PVA is sensitive to humidity. By varying environment temperature and humidity, the fiber achieved humidity sensitivities of −0.128 and 0.038 nm/%, while temperature sensitivities of 0.022 and −0.722 nm/°C. In addition to PDMS, aromatic polyimides (PIs) represent a significant category of heteroaromatic polymers known for their outstanding thermal stability, robust mechanical strength, high toughness, and low permittivity. Among these PIs, *p*-Phenylene biphenyltetracarboximide (BPDA-PDA) is sensitive to temperature with highest modulus, highest glass transition temperature, and lowest

* Corresponding author.

E-mail address: linchen@usst.edu.cn (L. Chen).

<https://doi.org/10.1016/j.optcom.2024.130362>

Received 30 November 2023; Received in revised form 27 January 2024; Accepted 2 February 2024

Available online 3 February 2024

0030-4018/© 2024 Elsevier B.V. All rights reserved.

coefficient of thermal expansion (CTE) value [22]. Although the optical sensors have been shown to be capable of parameters detection in complex environments, challenges remain in terms of their limited sensitivities, parameter interferences and fabrication cost. For example, thin functional coatings or thin optical fibers tend to offer a faster response with a lower sensitivity [11].

Metasurfaces are arrays of artificial structures consisting of periodic sub-wavelength units designed to be arranged in a two-dimensional plane. Based on the excellent performance of flexible design, easy integration, and powerful functions, metasensors are applied in applications of concentration detection [23], fingerprint recognition [24], medical diagnosis [25], absorber [26] and environment detection [19, 27]. In 2022, Yu [19] et al. proposed an all-dielectric metasensor for simultaneous measurement of temperature and humidity, and PDMS/PVA supported the sensing properties of temperature and humidity respectively. By studying the frequency shifts of the two resonance dips in transmission spectrum, the humidity sensitivities at both dips are -0.618 and -0.521 nm/%, while the temperature sensitivities are -0.224 and -0.069 nm/ $^{\circ}$ C. Current metasensors can be classified into dielectric and plasmonic depending on the materials. In all-dielectric metasensor in Ref. [19], electric and magnetic resonances are well-separated and can be easily distinguished, which benefits transmission phase control [28]. Consequently, plasmonic metasensors exhibit higher sensitivity and contrast to environmental parameters changes, making them better suited for deployment as environmental sensing devices [29]. Terahertz (THz) waves typically cover the frequency band of 0.1–10 THz, located between the microwave and infrared regions of the electromagnetic spectrum. In comparison to infrared and microwave waves, Terahertz (THz) waves typically cover the frequency band of 0.1–10 THz, located between the microwave and infrared regions of the electromagnetic spectrum. In comparison to infrared and microwave waves, THz wave is more capable of non-destructive detection and biomedicine due to its low photon energy, distinctive absorption spectra and intense resonant oscillations of various intermolecular vibrational and rotational modes within the molecules. Numerous reports about THz metasensors have been proposed for substance identification, trace detection and environmental testing [30–33]. In practical detection, RH can impact the rate of molecular diffusion and chemical reaction, leading to a remark influence in applications of non-destructive testing and chemical identification in THz band [34,35]. Additionally, intense temperature changes will influence the permittivity of medium materials, changing in dispersion and transmittance of transmitted THz waves. This characteristic will influence the sensing performance by impacting noise level in the sensor [36]. To our knowledge, there are few dual parameter sensors for a simultaneous measurement of RH and temperature reported in THz band. However, for applicability in complex environments and accuracy of measurement results, the measurement of RH and temperature in THz band should be further studied at the same time.

In this work, we demonstrate a metasensor for a simultaneous measurement of RH and temperature in THz band. The sensor is based on BPDA-PDA substrate and dual symmetrical golden rings, resulting in a special plasmonic resonant phenomena called electromagnetic induced transparency (EIT) with dual environment-sensitive resonance dips. For sensitivity calculation, the 14 μ m PVA is put on the sensor. By keeping the temperature (humidity) as a constant, the shifts of the resonance frequencies are linearly related to the humidity (temperature). Moreover, it is demonstrated that the effects of temperature and humidity on frequency shifts are independent, indicating that it can be optimized for applications involving simultaneous changes in both parameters. For feasible practical applications, we have given experimental design schemes, which has been proven in our previous work [37,38]. To our knowledge, this work is the first time to propose metasensor in THz band for simultaneous detection of temperature and humidity, which will exhibit more extraordinary properties in practical THz applications.

2. Structure design and analysis

The sensing properties of plasmonic metasensor are considered at normal incidence by vertically (y) polarized terahertz waves, and the sensing performance is proven insensitive to the incident and polarization angle shown in Fig. S1 (b),(d) in Supporting Information. Fig. 1(a) shows a schematic diagram of the proposed metasensor, which consists of two layers. The upper layer is composed of periodic golden arrays with the thickness of 100 nm, whose conductivity is $\delta = 4.56 \times 10^7$ S/m. The bottom layer is a lossy substrate of BPDA-PDA with $\epsilon = 2.955$ and its loss tangent angle is 0.0027 at $T = 25$ $^{\circ}$ C [39]. As seen in Fig. 1(b), the unit cell with periodic dimension $P = 200$ μ m is constructed by a pair of concentric golden rings, the width of each ring is $w = 7$ μ m and the inner radii of both rings are $R_1 = 63$ μ m and $R_2 = 83$ μ m, respectively. Numerical calculations are carried out using CST Microwave Studio 2019, a full-wave electromagnetic software that employs the finite integration technique to solve discrete Maxwell equations. Periodic boundary conditions are applied in the x and y directions, while the fully matched layer is utilized in the wave propagation direction z. Furthermore, local mesh refinements are applied specifically for the resonators to accurately capture the enhanced electric field near them. The mechanism of EIT can be explored by equivalent circuit resonance model. As seen in Fig. 2 (a), both ring resonators are considered as RLC circuit. Loop 1 (corresponding to small ring) consists of capacitor C_1 , inductor L_1 , resistor R_1 , power supply V_1 and coupling capacitor C_M , similar situation happens to Loop 2 (corresponding to large ring). Since two ring resonators can be coupling with each other, the coupling capacitances C_M are introduced into the circuit, which can be calculated from the standard expression for the asynchronously-tuned coupled resonators. According to superposition theorem, the whole excitation source of the circuit system is $u = v_1 - v_2 = V_1 e^{j\omega t} - V_2 e^{j\omega t} = V e^{j\omega t}$. The voltage and current equations of loops can be calculated by Kirchhoff Circuit Laws:

$$i_1(j\omega L_1 + 1/j\omega C_1 + 1/j\omega C_M + R_1) - i_2/j\omega C_M = v_1 \quad (1)$$

$$i_2(j\omega L_2 + 1/j\omega C_2 + 1/j\omega C_M + R_2) - i_1/j\omega C_M = v_2 \quad (2)$$

There is an assumption as follows: $i_1 = \dot{q}_1(t)$, $i_2 = \dot{q}_2(t)$, $q_1(t) = N_1 e^{-i\omega t}$, $q_2(t) = N_2 e^{-i\omega t}$, $\gamma_i = R_i/L_i$, $\omega_i^2 = 1/(L_i C_{ei})$, $C_{ei} = C_i C_M / (C_i + C_M)$ ($i = 1, 2$), $L_1 = L_2$, $\Omega_r^2 = 1/(L_1 C)$. Thus:

$$q_1''(t) + \gamma_1 \dot{q}_1(t) + \omega_1^2 q_1(t) - \Omega_r^2 q_2(t) = \frac{V_1}{L_1} e^{j\omega t} \quad (3)$$

$$q_2(t) + \gamma_2 \dot{q}_2(t) + \omega_2^2 q_2(t) - \Omega_r^2 q_1(t) = \frac{V_2}{L_2} e^{j\omega t} \quad (4)$$

The polarization rate of the circuit is $\chi = (g_1 q_1 + g_2 q_2) / (V_e \omega)$. Here g_1 , g_2 are coupling coefficient of two loops. The transmittance can be calculated by $1 - \text{Im}[\chi]$:

$$1 - \text{Im}[\chi] = 1 - K \text{Im} \left[\frac{(\omega^2 - \omega_2^2)^2 + i\omega\gamma_2}{\Omega^4 - (\omega^2 - \omega_2^2 + i\omega\gamma_2)(\omega^2 - \omega_1^2 + i\omega\gamma_1)} \right] \quad (5)$$

Here, the real part ($\text{Re}[\chi]$) represents the dispersion and the imaginary part ($\text{Im}[\chi]$) gives the absorption losses in the EIT system, K is the normalizing constant. $1 - \text{Im}[\chi]$ represents the transmission response of the system for the appropriate fitting parameters of $\omega_1, \omega_2, \gamma_1, \gamma_2$, and Ω . As seen in Fig. 2 (b), there is a calculated EIT-shape transmission obtained by equivalent circuit, and the corresponding circuit parameters are as follows: $C_1 = 0.32$ pF, $C_2 = 0.18$ pF, $L_1 = 0.5$ pH, $L_2 = 0.5$ pH, $R_1 = 9.4$ Ω , $R_2 = 13.7$ Ω .

Fig. 1 (c) shows the transmission spectra of single large ring, single small ring and concentric rings, respectively. In which there are two resonance dips at frequencies of 0.416 and 0.619 THz corresponding to the single large ring and single small ring, respectively. By combining two rings together, there is a slight frequency shift of resonance dip corresponding to single ring. In detail, there is a shift from 0.416 THz to

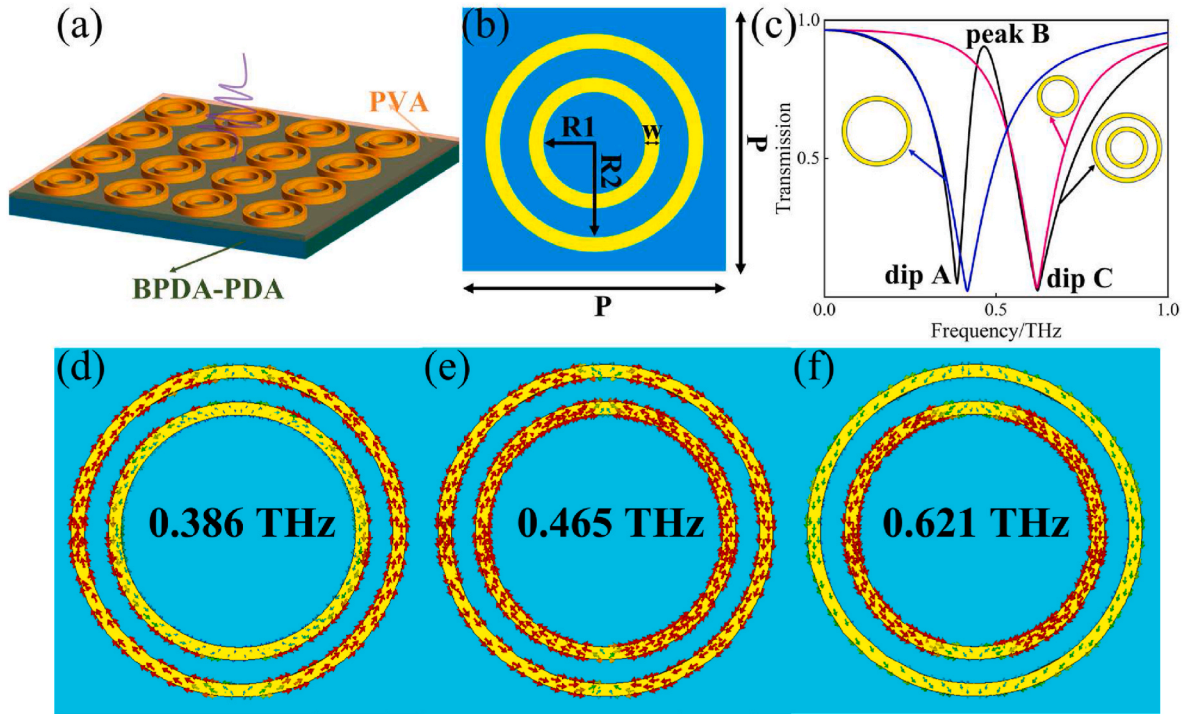


Fig. 1. (a) A schematic diagram of the metasensor. (b) The unit cell with detailed structural parameters: $P = 200 \mu\text{m}$, $R1 = 63 \mu\text{m}$, $R2 = 83 \mu\text{m}$, $w = 7 \mu\text{m}$. (c) The transmission spectra with single small ring, single large ring and concentric rings, respectively. The surface current distributions at (d) 0.386 THz (remarked dip A), (e) 0.465 THz (remarked peak B) and (f) 0.621 THz (remarked dip C), respectively.

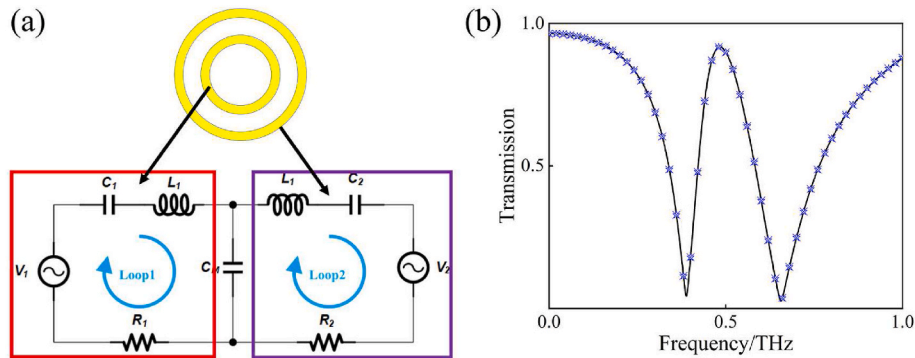


Fig. 2. (a) The equivalent circuit of EIT effect. (b) The theoretical calculation of transmission by equivalent circuit.

0.386 THz (remarked as dip A) corresponding to large ring, and a shift from 0.619 THz to 0.621 THz (remarked as dip C) corresponding to small ring. Meanwhile, rings with different radii supports corresponding different electric dipole resonances, which can be regarded as bright-mode resonators. When both bright-mode resonators are coupled, a transparency window occurs at a frequency of 0.465 THz (referred to as peak B), leading to the formation of electromagnetic induced transparency (EIT) in the spectrum. Except bright-dark model coupling for EIT construction, bright-bright model coupling for EIT has been proposed [40]. For a further explanation of EIT mechanism, the surface current distributions at both dips and peak are demonstrated in Fig. 1 (d)–(f). The dipole mode of outer (inner) ring makes a dominant contribution to the resonance at 0.386 (0.621) THz. In other hand, there are two exclusionary electric dipole resonances with a phase difference of 180° at dip A. While at dip C, phase difference disappears and there is higher resonance frequency among electrical dipoles for inner and outer rings. At peak B, the currents in both rings are reversed, resulting in destructive interference between dipoles of inner and outer rings and significant transparency peak. Additionally, we have optimized the

structural parameters to $R1 = 60 \mu\text{m}$ and $R2 = 86 \mu\text{m}$ for better sensing performance by scanning parameters of $R1$ and $R2$ in Fig. S1 (a),(c) in Supporting Information. Besides, the designed sensor is polarization insensitive over 90° angle variation, while over 80° for incident wave, proving extraordinary stability and suitability seen in Fig. S1 (b),(d) in Supporting Information.

3. Numerical demonstration for dual-parameter sensor

The thickness of analyte is a vital factor for frequency shift, which should be discussed. PVA with different thicknesses ranging from 4 to $16 \mu\text{m}$ is put on the metasensor at $T = 25^\circ\text{C}$, and the frequency shifts on both resonance dips are demonstrated in Fig. 3 (a). There is a slight influence of analytes thickness on resonance frequencies. For a precise influence of thermal expansion on the sensor, when temperature increases to 65°C , the thicknesses of PVA, gold film and BPDA-PDA increase 0.19, 5.68×10^{-5} and $0.036 \mu\text{m}$, respectively (corresponding thermal expansion of coefficients are listed in Table 1). The thickness of PVA is proved independent to frequency shift, while tiny expansion of

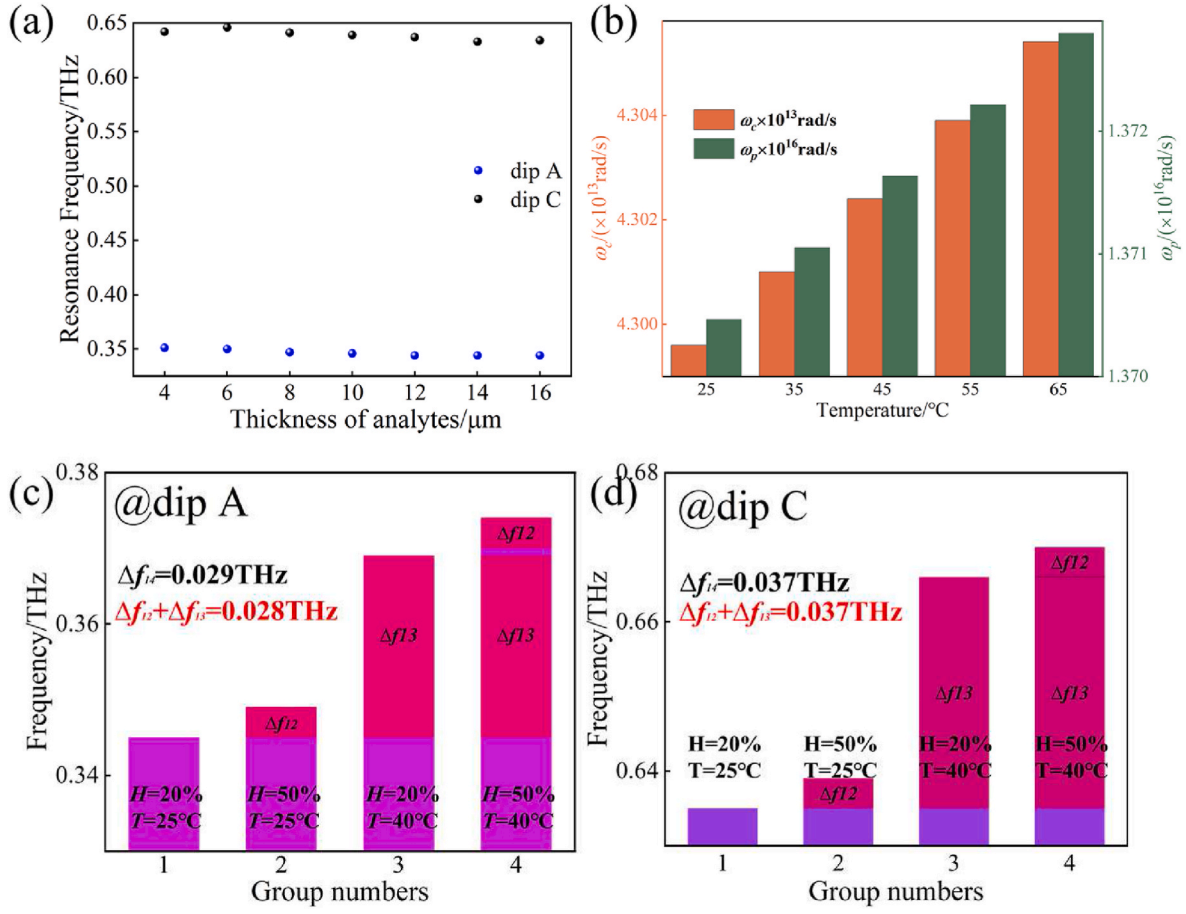


Fig. 3. (a) The impact of PVA thickness on frequency shifts at both dips. (b) Calculated ω_c and ω_p over a range of temperature from 25 to 65 °C. The independent influence of temperature and humidity at (a) dip A and (b) dip C.

Table 1

Thermal and optic parameters of given materials.

Material/parameter	PVA [19,45]	Gold film	BPDA-PDA [22]
TOC/°C ⁻¹	-2.16×10^{-4}	-	-8.68×10^{-3}
CTE/°C ⁻¹	3.4×10^{-4}	1.42×10^{-5}	3×10^{-5} – 7×10^{-5}

gold film and BPDA-PDA can be ignored. The permittivity of gold film can be described by Drude model [41]:

$$\varepsilon(T) = 1 - \frac{\omega_p^2}{\omega(\omega + j\omega_c)} \quad (6)$$

In which ω_p and ω_c are the plasma frequency and metal electron collision frequency, respectively. Both of them are related to temperature, which can be calculated by the following equations [42]:

$$\omega_p(T) = \omega_{p0} [1 + 3\gamma(T - T_0)]^{-1/2} \quad (7)$$

$$\omega_c(T) = \omega_{cp}(T) + \omega_{ce}(T) \quad (8)$$

In which γ represents CTE for the gold film. $T_0 = 27$ °C serves as the reference temperature, while $\omega_{p0} = 1.37 \times 10^{16}$ rad/s signifies the plasma frequency at 27 °C. The collision frequency of metal electrons can be decomposed into two components: electron-related frequency ω_{ce} and phonon-related frequency ω_{cp} . These parameters are determined utilizing the models proposed by Lawrence and Holstein [43,44]:

$$\omega_{cp}(T) = \omega_0 \left[\frac{2}{5} + \frac{4\Gamma^5}{\theta_D^5} \int_0^{\frac{\omega_p}{T}} \frac{z^4}{e^z - 1} dz \right] \quad (9)$$

$$\omega_{ce}(T) = \frac{\pi^3 \Gamma \Delta}{12 \hbar E_f} \left[(k_B T)^2 + \left(\frac{\hbar \omega}{2\pi} \right)^2 \right] \quad (10)$$

In which $\omega_0 = 1.07 \times 10^{13}$ rad/s is collision frequency, $\Gamma = 0.55$ is average of scattering probability, $\Delta = 0.77$ is fractional Umklapp scattering, $\theta_D = -93$ °C is Debye temperature, $E_f = 5.51$ eV is Fermi level, $k_B = 1.38062 \times 10^{-23}$ J/°C is Boltzmann constant, and $\hbar = 1.0546 \times 10^{-34}$ J·s is Planck constant. According to Eqs. (1)–(5), the calculated ω_p and ω_c are demonstrated in Fig. 3 (b).

Next, the independent influence of both temperature and humidity on frequency shifts are discussed. The method of incorporating the effect of humidity changes into the simulation environment is based on the fact that the PVA is sensitive to environment humidity. A quantitative approach to incorporating this effect in the simulation is as follows. When the environment humidity changes, the refractive index of PVA has a linear reduction, which corresponds to the humidity coefficient of PVA (-1.44×10^{-3} RIU/%) [19]. That is to say, when relative humidity increases 10%, the refractive index of PVA decreases 1.44×10^{-2} , whose influence on frequency shifts can be calculated in CST software. In addition, the effect of humidity on the substrate (BPDA-PDA) refractive index can be ignored in modelling due to its relatively dense molecular structure which contains numerous aromatic rings and bonds in its internal structure [22]. There are four sets of simulation environment, as seen in Fig. 3(c), (d). Group 1 is set to $T = 25$ °C and $H = 20\%$, group 2 is set to $T = 25$ °C and $H = 50\%$, group 3 is set to $T = 40$ °C and $H = 20\%$, and group 4 is set to $T = 40$ °C and $H = 50\%$. For a better view of frequency shifts, there is a definition that Δf_{i1} means frequency shifts on both dip A and dip C when environment setting changes from group 1 to group i . For dip A seen in Fig. 3(c), by contrasting group 1 to group 2,

there is a slight blueshift (Δf_{12}) caused by ΔH ; by contrasting group 1 to group 3, there is a marked blueshift (Δf_{13}) caused by ΔT ; by contrasting group 1 to group 4, there is a marked blueshift (Δf_{14}) caused by ΔT and ΔH simultaneously. We have calculated that $\Delta f_{12} + \Delta f_{13} = 0.028$ THz, while $\Delta f_{14} = 0.029$ THz, that is to say, the effect of temperature and humidity on frequency shifts is independent within error limits of 0.001 THz. Similar situation happens in frequency shift at dip C ($\Delta f_{12} + \Delta f_{13} = \Delta f_{14} = 0.037$ THz), as seen in Fig. 3(d). Then the designed sensor can achieve detection of environment parameters (temperature and humidity) variation simultaneously. When the temperature and humidity of external environment change, the resonance frequencies at both dips will have shifts unevenly. So the response of the sensor is due to the combination of two parts: the changes of environment temperature and humidity, which can be calculated by Ref. [46]:

$$\frac{\partial f_i}{\partial H} \times \Delta H + \frac{\partial f_i}{\partial T} \times \Delta T = \Delta f_i \quad (i = 1, 2) \quad (11)$$

Where $i = 1, 2$ represent dip A and dip C, respectively. $\partial f_i / \partial H$ represents the rate change of frequency caused by humidity, and $\partial f_i / \partial T$ represents the rate change of frequency caused by temperature. Converting Eq. (11) to matrix form as follows:

$$\begin{bmatrix} \frac{\partial f_1}{\partial H} & \frac{\partial f_1}{\partial T} \\ \frac{\partial f_2}{\partial H} & \frac{\partial f_2}{\partial T} \end{bmatrix} \begin{bmatrix} \Delta H \\ \Delta T \end{bmatrix} = \begin{bmatrix} K_{H,1} & K_{T,1} \\ K_{H,2} & K_{T,2} \end{bmatrix} \begin{bmatrix} \Delta H \\ \Delta T \end{bmatrix} = \begin{bmatrix} \Delta f_1 \\ \Delta f_2 \end{bmatrix} \quad (12)$$

where $\mathbf{K} = \begin{bmatrix} K_{H,1} & K_{T,1} \\ K_{H,2} & K_{T,2} \end{bmatrix}$ is the sensitivity coefficient matrix, which is independent of the ambient temperature change ΔT and the humidity change ΔH . The \mathbf{K} matrix can be demarcated by environment detection.

Here we discuss how changes in ambient temperature affect the variations in the refractive index of BPDA-PDA substrate due to the thermo-optic effect. The thermal-optic coefficient of substrate (BPDA-PDA) is -8.68×10^{-3} RIU/ $^{\circ}\text{C}$ which listed in Table .1, indicating that the refractive index of the substrate decreases 8.68×10^{-2} when the temperature increases by 10°C . Such variations in the substrate refractive index due to the thermo-optic effect has been considered in our simulation and has been listed in our initial supplementary materials. To see this point clearly, we shifted this discussion from supplementary materials to manuscript. We have analyzed the effect of temperature on frequency shifts without PVA in Fig. 4 (a), there is a remarkable frequency shift from 0.386 (0.621) THz to 0.452 (0.723) THz at dip A (dip C), showing that BPDA-PDA is a temperature-sensitive material for temperature sensing. The influence of temperature on BPDA-PDA substrate causes remarkable blue shifts at dual resonance dips. We have also separately investigated the effect of the BPDA-PDA, PVA and gold film components on the frequency shifts when the temperature rises 10°C . The average frequency shifts are seen in Fig. 4 (b), (c), with positive values indicating blue shifts and negative values indicating red shifts. So the influence of temperature on PVA and gold

film causes slight red shifts at dual resonance dips and the temperature sensing is dominated by BPDA-PDA.

For a solution of humidity sensitivity, the environment temperature is stable at 25°C , and a range of humidity is from 20% to 60% with a step of 10%, in total five groups. When the environment humidity changes, the refractive index of PVA has a linear reduction, which corresponds to the humidity coefficient of PVA. As seen in Fig. 5 (a), there are frequency shifts at both dip A and dip C with the change of environment humidity. When humidity increases from 20% to 60%, there are blue shifts from 0.345 to 0.351 THz at dip A and from 0.631 to 0.642 THz at dip C. Fig. 5 (b) shows linear relationship between humidity and frequency shifts, which indicates that $K_{H,1}$ is 0.14 GHz/% and $K_{H,2}$ is 0.27 GHz/%. Similarly for temperature sensitivity, environmental humidity remains at 30%, and temperature varies from 25 to 65°C with a step of 10°C . As seen in Fig. 5 (c), there are frequency shifts at both dip A and dip C with the change of environment temperature. When temperature increases from 25°C to 65°C , there is a blue shift from 0.345 to 0.399 THz at dip A, while from 0.631 to 0.729 THz at dip C. Fig. 5 (d) shows the linear relationship between temperature and frequency shifts, which indicates that $K_{T,1}$ is 1.35 GHz/ $^{\circ}\text{C}$ and $K_{T,2}$ is 2.45 GHz/ $^{\circ}\text{C}$. The resonance frequencies in our designed EIT effect are 0.386 and 0.621 THz, respectively, and EIT peak is at 0.465 THz. However, two strong water-vapor absorption peaks are located at 0.557 and 0.755 THz [47]. The resonance dips and EIT peak avoid water-vapor absorption peaks, leading to a slight influence on EIT sensor. So in practical scenarios, a background noisy signal may not heavily distort the response during 40% or 60% humidity cases. This conclusion had already been verified by Kim et al. [3]. They had proposed a THz metasensor for humidity sensing experimentally, in which the environment humidity is up to 78%, and the background noisy signal caused by high humidity does not distort sensing response [48].

The \mathbf{K} matrix now can be calculated in Eq. (11). The designed sensor is sensitive to environment temperature and humidity simultaneously. All above discussions are based on the premise of controlling a single variable, showing a linear change in humidity (or temperature) when the temperature (or humidity) is constant. In this case, we obtain that the frequency shifts are linearly related to temperature and humidity when they are varied singularly.

$$\begin{bmatrix} K_{H,1} & K_{T,1} \\ K_{H,2} & K_{T,2} \end{bmatrix} \begin{bmatrix} \Delta H \\ \Delta T \end{bmatrix} = \begin{bmatrix} 0.14 & 0.27 \\ 1.35 & 2.45 \end{bmatrix} \begin{bmatrix} \Delta H \\ \Delta T \end{bmatrix} = \begin{bmatrix} \Delta f_1 \\ \Delta f_2 \end{bmatrix} \quad (13)$$

The sensitivities in terms of wavelength are $\partial \lambda_i / \partial T (\partial \lambda_i / \partial H) = -c / f_0^2 \times \partial f_i / \partial T (\partial f_i / \partial H)$, where $c = 3 \times 10^8$ m/s and $f_0 = 0.386$ and 0.621 THz are both dip A and dip C without analyte [49]. The \mathbf{K} matrix corresponding to wavelength is as follows:

$$\begin{bmatrix} K_{H,1} & K_{T,1} \\ K_{H,2} & K_{T,2} \end{bmatrix} \begin{bmatrix} \Delta H \\ \Delta T \end{bmatrix} = \begin{bmatrix} -282 & -210 \\ -2718 & -1906 \end{bmatrix} \begin{bmatrix} \Delta H \\ \Delta T \end{bmatrix} = \begin{bmatrix} \Delta \lambda_1 \\ \Delta \lambda_2 \end{bmatrix} \quad (14)$$

Inverse the matrix in Eqs. (11) and (12) and the calculation of ΔT and ΔH are as follows. When the environment temperature and RH change

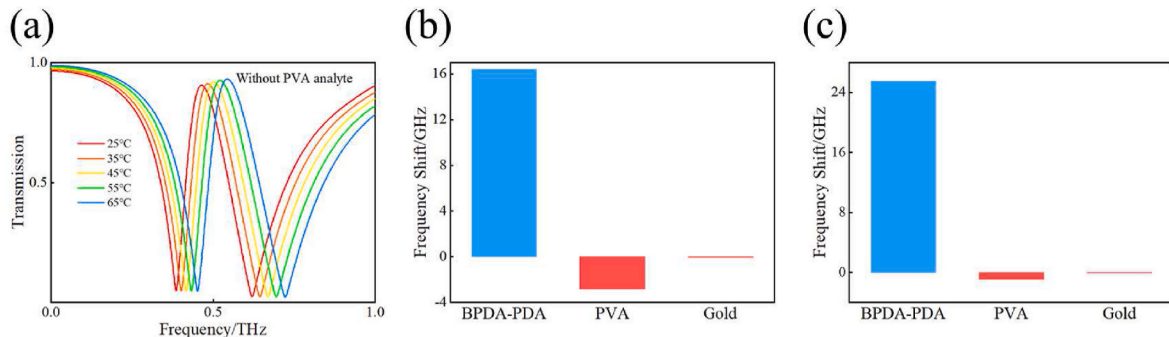


Fig. 4. (a) The influence of temperature on frequency shifts without PVA analyte. Frequency shifts caused by respective factors at dip A (b) and dip C (c).

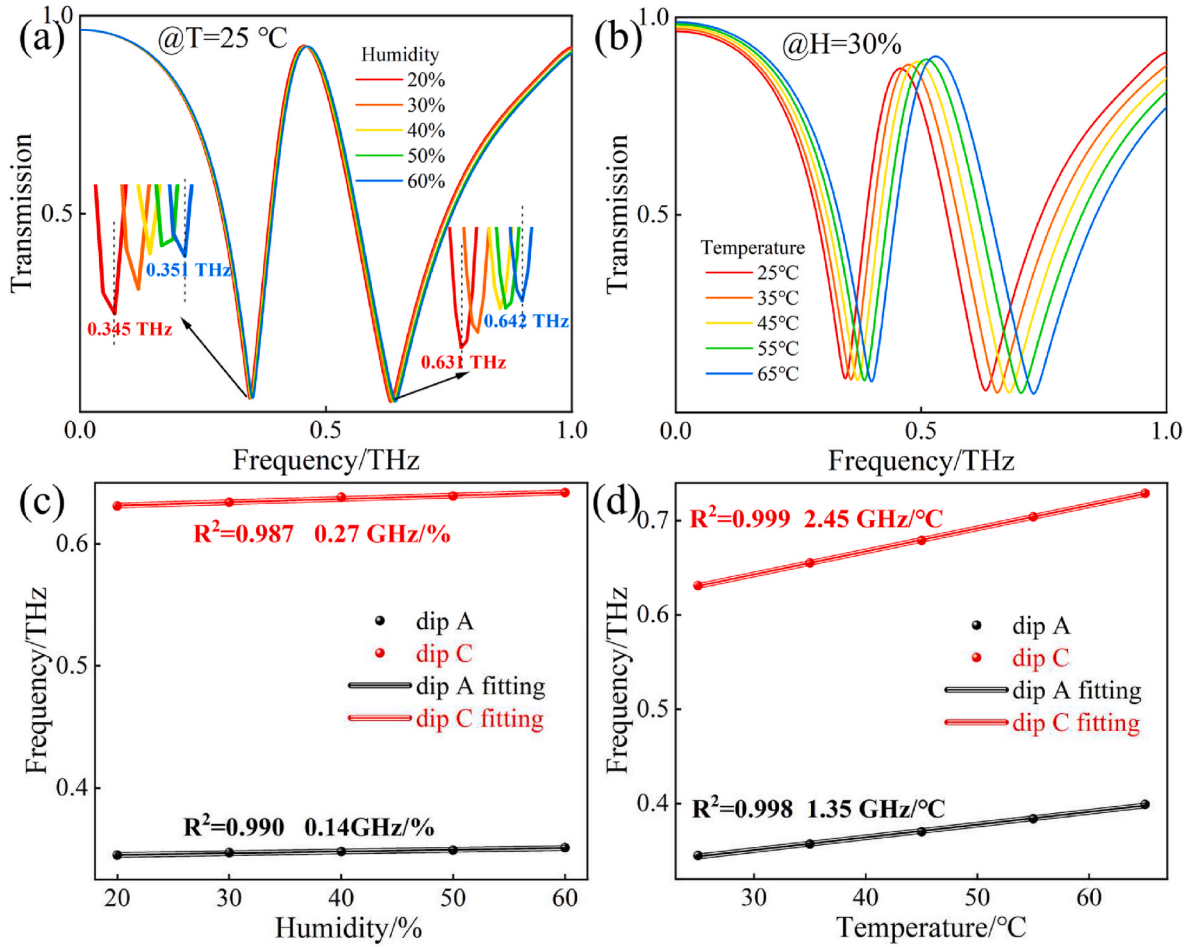


Fig. 5. (a) The transmission spectra at different humidity. (b) Sensitivity of frequency shifts on temperature. (c) The transmission spectra at different humidity. (d) Sensitivity of frequency shifts on temperature.

simultaneously, there is need to measure frequency or wavelength shifts at dip A and dip C, and the corresponding temperature and RH changes can be calculated by Eqs. (15) and (16).

$$\Delta T = \frac{2.45\Delta f_1 - 0.27\Delta f_2}{-0.0215} = \frac{1906\Delta\lambda_1 - 210\Delta\lambda_2}{-33288} \quad (15)$$

$$\Delta H = \frac{0.14\Delta f_2 - 1.35\Delta f_1}{-0.0215} = \frac{282\Delta\lambda_2 - 2718\Delta\lambda_1}{-33288} \quad (16)$$

4. Feasible experimental design

BPDA-PDA can be made by electrospinning a solution of the PI precursor, *p*-phenylene biphenyl tetracarboxamide acid, in dimethyl acetamide [22]. The metasensors can be fabricated by liftoff lithography [23,24]. PVA and five saturated salt solutions (lithium chloride, potassium acetate, magnesium bromide, magnesium chloride, potassium carbonate, magnesium nitrate) can be provided by Shanghai Aladdin biochemical Technology. Their solution configuration procedures are available in Ref. [15]. Then the PVA solution is dropped on designed sensor evenly, and the entire sensor is put into a furnace with a controlled stable temperature at 50 °C for 3 hours to solidify the sensitive material. Five saturated salt solutions can achieve the humidity change of environment [21], and the detailed humidity corresponding to solutions are listed in Table 2. There are possible humidity errors in practical experiment, so a hygrometer (RotronicHC2-S (3)) for precise humidity is necessary. THz time-domain spectroscopy system can be used to obtain time and frequency spectra with operation frequency ranges from 0 to 3 THz, the signal dynamic range 60 dB, and the spectral

Table 2

Correspondence of RH and saturated salt solutions with different temperature [51].

	LiCl·H ₂ O	MgCl ₂ ·6H ₂ O	Na ₂ Cr ₂ O ₇ ·2H ₂ O	NaCl	KNO ₃
15 °C	12.8%	33.9%	56.6%	75.3%	94.4%
20 °C	12.4%	33.6%	55.2%	75.5%	93.2%
25 °C	12.0%	33.2%	53.8%	75.8%	92.0%
30 °C	11.8%	32.8%	52.5%	75.6%	90.7%
35 °C	11.7%	32.5%	51.2%	75.5%	89.3%

resolution 7.6 GHz. Besides, a commercial heater board with a size of 15 mm × 15 mm is necessary for temperature change, whose temperature ranges from 25 to 120 °C. Different environment humidity caused by various saturated salt solutions can be achieved by microfluidic chip. As seen in Fig. 6 (a), by fixing the sensor to the 8 mm quartz base, different saturated salt solutions were evenly dripped onto the sensor surface by a dropper [23]. Then the sensor is put into a climatic chamber (CVMS Climatic, Benchtop C-TH40, UK) and remains a constant temperature [12]. For a precise result, hygrometer is necessary for each experimental group. Various salt solutions demonstrate different environment humidity, the humidity sensitivity can be obtained by measuring the ratio of the humidity change to the frequency shifts according to theory in section 3. A tunable temperature condition can be achieved by a heater board shown in Fig. 6 (b), in piratical experiment, a heat-conducting plate with through-hole is fixed on the heater board, and the sensor is just placed on the through hole. Here a heater with a sample holder or clamp is used to uniformly heat the sample and parallelly acquire the

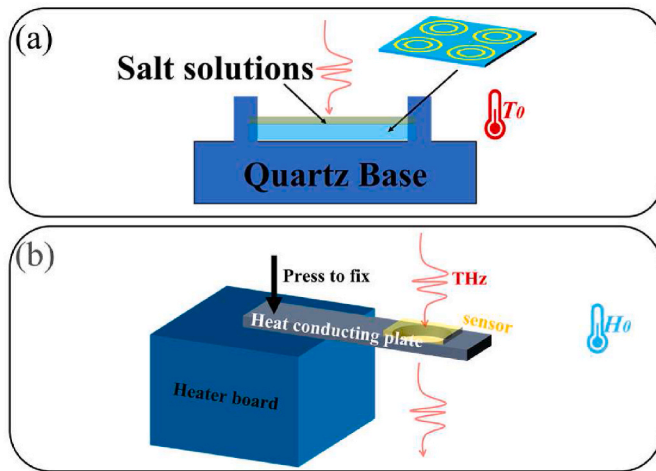


Fig. 6. (a) Humidity and (b) temperature experiment schemas.

transmission spectrum [50]. With temperature increases, there are blue shifts at both resonance dips. Considering that humidity change can affect temperature sensitivity, and content humidity should be controlled and fluctuated by 1%. Then temperature sensitivity will be demonstrated experimentally.

5. Discussions and conclusions

The precise control of humidity is indispensable in diverse applications, while it has a subtle connection with temperature. Now a hybrid sensor for simultaneous measurement of temperature and RH should be demonstrated. In this work, a plasmonic metasensor is demonstrated based on EIT for the environment detection. Both dipole resonances are capable of coupling with each other, result in EIT effect. Both resonance dips at the EIT transmission are sensitive to tiny environmental (humidity and temperature) changes, which is determined by specific construction, unique materials and high frequency. The designed metasensor is polarization insensitive and incidence insensitive (over 80°). For the humidity sensor, we maintain a constant temperature of 25°C and change the humidity values in five groups from 20% to 60%. Results show that the linear relationship between RH and frequency shifts. The humidity sensitivity is $0.14\text{ GHz}/\%$ at low frequency (dip A) and 0.27

$\text{GHz}/\%$ at high frequency (dip C). A similar situation occurs for temperature sensing. The RH remains at 30% by changing the temperature values from 25 to 65°C in five groups. Results also show the linear relationship between temperature and humidity, with a sensitivity of $1.35\text{ GHz}/^\circ\text{C}$ at dip A, and $2.45\text{ GHz}/^\circ\text{C}$ at dip C. For practical applications, the complete experimental procedures and related precautions are discussed. Table 3 lists performances of various dual-parameter sensors. Ref. [19,21,52] cover a performance of simultaneous measurement of temperature and RH with different structures in infrared band. Single sensing properties (RH or temperature) are performed in THz band, lacking of applicability in variable environment of RH and temperature simultaneously [20,27,36,48,53]. Our proposed metasensor exhibit high sensitivities and versatilities. To our knowledge, this is the first time to realize simultaneous measurement of temperature and RH in THz band, which has potential application scenarios in THz technologies [54,55].

Funding

This work was supported in part by the Basic Science Center Project of the National Natural Science Foundation of China (Grant No. 61988102), National Natural Science Foundation of China (grant no. 62275157), the Shanghai Shuguang Program, China (Grant No. 18SG44), 111 Project (grant no. D18014).

CRediT authorship contribution statement

QianRu Ma: Writing – original draft, Visualization, Validation, Investigation, Data curation, Conceptualization. **Yi Ma:** Writing – original draft, Visualization, Validation, Software, Resources, Methodology, Investigation, Formal analysis, Data curation, Conceptualization. **ZeShuai Ren:** Investigation, Formal analysis, Conceptualization. **Lin Chen:** Writing – review & editing, Writing – original draft, Supervision, Software, Project administration, Methodology, Investigation, Funding acquisition, Formal analysis, Data curation, Conceptualization.

Declaration of competing interest

The authors declare the following financial interests/personal relationships which may be considered as potential competing interests: Lin Chen reports financial support was provided by Basic Science Center Project of the National Natural Science Foundation of China. Lin Chen

Table 3
Comparison with other fabricated RH and temperature sensors.

Ref	RH_A	RH_C	T_A	T_C	Realization	Operation band
[21] (2022)	$-0.128\text{ nm}/\%$	$0.038\text{ nm}/\%$	$0.022\text{ nm}/^\circ\text{C}$	$-0.722\text{ nm}/^\circ\text{C}$	FPI (Experimentally)	1530–1570 nm
[52] (2021)	$0.43\text{ nm}/\%$	–	$3.97\text{ nm}/^\circ\text{C}$	–	TLC (Experimentally)	200–1000 nm
[27] (2020)	–	–	$6.35\text{ MHz}/^\circ\text{C}$	$7.14\text{ MHz}/^\circ\text{C}$	PM (Numerically)	0–1.2 THz
[36] (2023)	–	–	$0.95\text{ GHz}/^\circ\text{C}$	$1.22\text{ GHz}/^\circ\text{C}$	PM (Numerically)	0–2 THz
[53] (2017)	–	–	$1400\text{ nm}/\text{K}$	–	MZI (Experimentally)	300–340 μm
[48] (2018)	–	$0.22\text{ GHz}/\%$	–	–	PM (Experimentally)	0.7–0.8 THz
[20] (2023)	–	$0.34\text{ GHz}/\%$	–	–	PM (Numerically)	0.72–0.78 THz
[19](2022)	$-0.618\text{ nm}/\%$	$-0.521\text{ nm}/\%$	$-0.224\text{ nm}/^\circ\text{C}$	$-0.069\text{ nm}/^\circ\text{C}$	DM (Numerically)	1450–1750 nm
Our work	$0.14\text{GHz}/\%$ ($-282\text{ nm}/\%$)	$0.27\text{GHz}/\%$ ($-210\text{ nm}/\%$)	$1.35\text{ GHz}/^\circ\text{C}$ ($-2718\text{ nm}/^\circ\text{C}$)	$2.45\text{ GHz}/^\circ\text{C}$ ($-1906\text{ nm}/^\circ\text{C}$)	PM (Numerically)	0–1 THz

*FPI: Fabry–Perot Interferometer.

*TLC: Thermochromic Liquid Crystal.

*MZI: Mach-Zehnder Interferometer.

*PM: Plasmonic Metasensor.

*DM: Dielectric Metasensor.

reports financial support was provided by National Natural Science Foundation of China. Lin Chen reports financial support was provided by the Shanghai Shuguang Program. Lin Chen reports financial support was provided by 111 Project.

Data availability

Data will be made available on request.

Appendix A. Supplementary data

Supplementary data to this article can be found online at <https://doi.org/10.1016/j.optcom.2024.130362>.

References

- [1] T.G. Hoffmann, C. Meinert, F. Ormelez, et al., Fresh food shelf-life improvement by humidity regulation in domestic refrigeration, *Procedia Comput. Sci.* 217 (2023) 826–834.
- [2] G. Guarnieri, B. Olivieri, G. Senna, et al., Relative humidity and its impact on the Immune system and Infections, *Int. J. Mol. Sci.* 24 (2023), <https://doi.org/10.3390/ijms24119456>.
- [3] J.K. Zuur, S.H. Muller, F.H.C. de Jongh, et al., The physiological rationale of heat and moisture exchangers in post-laryngectomy pulmonary rehabilitation: a review, *European Archives of Oto-Rhino-Laryngology and Head & Neck* 263 (1) (2006) 1–8.
- [4] D.L. Presti, C. Massaroni, J. D'Abbraccio, et al., Wearable system based on flexible FBG for respiratory and cardiac monitoring, *IEEE Sensor. J.* 19 (17) (2019) 7391–7398.
- [5] Y. Wang, W. Yuan, Y. Yan, et al., Signal processing integrated with fiber-optic Vernier effect for the simultaneous measurement of relative humidity and temperature, *Opt Express* 31 (17) (2023) 28636–28648.
- [6] Z. Dong, Y. Jin, G. Zhang, et al., Single core-offset Mach-Zehnder interferometer coated with PVA for simultaneous measurement of relative humidity and temperature, *Opt Express* 29 (15) (2021) 24102–24117.
- [7] Z. Han, J. Chao, Z. Xiping, et al., Simultaneous humidity and temperature measurement sensor based on two cascaded long-period fiber gratings, *Opt Commun.* 530 (2023) 129137.
- [8] H. Hammouche, H. Achour, S. Makhlof, et al., A comparative study of capacitive humidity sensor based on keratin film, keratin/graphene oxide, and keratin/carbon fibers, *Sensor Actuator Phys.* 329 (2021) 112805.
- [9] M.A. Najebe, Z. Ahmad, R.A. Shakoor, Organic thin-film capacitive and resistive humidity sensors: a Focus review, *Adv. Mater. Interfac.* 5 (21) (2018) 1800969.
- [10] S. Li, Y. Zhang, X. Liang, et al., Humidity-sensitive chemoelectric flexible sensors based on metal-air redox reaction for health management, *Nat. Commun.* 13 (1) (2022) 5416.
- [11] X. Rao, L. Zhao, L. Xu, et al., Review of optical humidity sensors, *Sensors* 21 (23) (2021) 8049.
- [12] D. Liu, Z. Cai, B. Li, et al., Simultaneous measurement of humidity and temperature based on fiber-tip microcantilever cascaded with fiber Bragg grating, *Opt Express* 31 (5) (2023) 8738–8747.
- [13] S. Pevec, D. Donlagic, Miniature all-fiber Fabry–Perot sensor for simultaneous measurement of pressure and temperature, *Appl. Opt.* 51 (19) (2012) 4536–4541.
- [14] J.-X. Li, Z.-R. Tong, L. Jing, et al., Fiber temperature and humidity sensor based on photonic crystal fiber coated with graphene oxide, *Opt Commun.* 467 (2020) 125707.
- [15] Y. Hu, A. Ghaffar, Y. Hou, et al., A micro structure POF relative humidity sensor Modified with Agarose based on surface plasmon resonance and Evanescent wave loss, *Photonic Sensors* 11 (4) (2021) 392–401.
- [16] D. Lopez-Torres, C. Elosua, J. Villatoro, et al., Photonic crystal fiber interferometer coated with a PAH/PAA nanolayer as humidity sensor, *Sensor. Actuator. B Chem.* 242 (2017) 1065–1072.
- [17] F.U. Hernandez, S.P. Morgan, B.R. Hayes-Gill, et al., Characterization and Use of a fiber optic sensor based on PAH/SiO₂ film for humidity sensing in Ventilator Care equipment, *IEEE (Inst. Electr. Electron. Eng.) Trans. Biomed. Eng.* 63 (9) (2016) 1985–1992.
- [18] C. Huang, W. Xie, D. Lee, et al., Optical fiber humidity sensor with porous TiO₂/SiO₂/TiO₂ coatings on fiber tip, *IEEE Photon. Technol. Lett.* 27 (14) (2015) 1495–1498.
- [19] Z. Yu, T. Lang, Z. Hong, et al., Sensors for simultaneous measurement of temperature and humidity based on all-dielectric metamaterials, *Opt Express* 30 (11) (2022) 18821–18835.
- [20] J. Gu, J. Qin, Z. Han, Relative humidity sensing using THz metasurfaces combined with polyvinyl alcohol, *Appl. Opt.* 61 (20) (2022) 6086–6091.
- [21] F. Li, X.g. Li, X. Zhou, et al., Simultaneous measurement of temperature and relative humidity using cascaded C-shaped fabry-perot interferometers, *J. Lightwave Technol.* 40 (4) (2022) 1209–1215.
- [22] Z. Wu, J. He, H. Yang, et al., Progress in aromatic polyimide films for electronic applications: preparation, structure and properties, *Polymers* 14 (2022), <https://doi.org/10.3390/polym14061269>.
- [23] W. Fu, L. Sun, H. Cao, et al., Qualitative and quantitative recognition of volatile organic compounds in their Liquid phase based on terahertz microfluidic EIT metasensors, *IEEE Sensor. J.* 23 (12) (2023) 12775–12784.
- [24] J. Lyu, S. Shen, L. Chen, et al., Frequency selective fingerprint sensor: the Terahertz unity platform for broadband chiral enantiomers multiplexed signals and narrowband molecular AIT enhancement, *PhotonX* 4 (1) (2023) 28.
- [25] F. Li, J. Shen, C. Guan, et al., Exploring near-field sensing efficiency of complementary plasmonic metasurfaces for immunodetection of tumor markers, *Biosens. Bioelectron.* 203 (2022) 114038.
- [26] Y. Zhang, T. Li, Q. Chen, et al., Independently tunable dual-band perfect absorber based on graphene at mid-infrared frequencies, *Sci. Rep.* 5 (1) (2015) 18463.
- [27] G. Wang, T. Lang, Z. Hong, Metallic metamaterial terahertz sensors for simultaneous measurement of temperature and refractive index, *Appl. Opt.* 59 (18) (2020) 5385–5390.
- [28] M.I. Shalaev, J. Sun, A. Tsukernik, et al., High-Efficiency all-dielectric metasurfaces for ultracompact beam manipulation in transmission mode, *Nano Lett.* 15 (9) (2015) 6261–6266.
- [29] T.T. Hoang, T.S. Pham, X.B. Nguyen, et al., High contrast and sensitive near-infrared refractive index sensors based on metal-dielectric-metal plasmonic metasurfaces, *Phys. B Condens. Matter* 631 (2022) 413469.
- [30] L. Huang, H. Cao, L. Chen, et al., Terahertz reconfigurable metasensor for specific recognition multiple and mixed chemical substances based on AIT fingerprint enhancement, *Talanta* 269 (2024) 125481.
- [31] Y. Ma, L. Huang, X. Wang, et al., Simultaneous detection of refractive index and temperature in terahertz band based on electromagnetic induced transparency effect, *IEEE Sensor. J.* 23 (19) (2023) 22476–22485.
- [32] J. Lyu, L. Huang, L. Chen, et al., Review on the terahertz metasensor: from featureless refractive index sensing to molecular identification, *Photon. Res.* 12 (2) (2024) 194–217.
- [33] Y. Zhang, T. Li, B. Zeng, et al., A graphene based tunable terahertz sensor with double Fano resonances, *Nanoscale* 7 (29) (2015) 12682–12688.
- [34] B. Wang, K. Meng, T. Song, et al., Qualitative detection of amino acids in a mixture with terahertz spectroscopic imaging, *J. Opt. Soc. Am. B* 39 (3) (2022) A18–A24.
- [35] G.R. Musina, N.V. Chernomyrdin, E.R. Gafarova, et al., Moisture adsorption by decellularized bovine pericardium collagen matrices studied by terahertz pulsed spectroscopy and solid immersion microscopy, *Biomed. Opt Express* 12 (9) (2021) 5368–5386.
- [36] Y.G. Zhang, Z.W. Feng, L.J. Liang, et al., High-performance dual-tunable terahertz absorber based on strontium titanate and bulk Dirac semimetal for temperature sensing and switching function, *Appl. Opt.* 62 (21) (2023) 5822–5829.
- [37] L. Chen, N. Xu, L. Singh, et al., Defect-induced fano resonances in corrugated plasmonic metamaterials, *Adv. Opt. Mater.* 5 (8) (2017) 1600960.
- [38] L. Chen, Y. Zhu, X. Zang, et al., Mode splitting transmission effect of surface wave excitation through a metal hole array, *Light Sci. Appl.* 2 (3) (2013) e60.
- [39] Y. Terui, S. Ando, Polarization dependence of thermo-optic coefficients in polyimide films originating from chain orientation and residual thermal stress, *J. Appl. Phys.* 116 (5) (2014) 053524.
- [40] H. Chen, H. Zhang, M. Liu, et al., Realization of Tunable Plasmon-Induced Transparency by Bright-Bright Mode Coupling in Dirac Semimetals, vol. 7, 2017, pp. 3397–3407.
- [41] I.T. Kim, K.D. Kihm, Full-field and real-time surface plasmon resonance imaging thermometry, *Opt Lett.* 32 (23) (2007) 3456–3458.
- [42] C.S. Moreira, A.M.N. Lima, H. Neff, et al., Temperature-dependent sensitivity of surface plasmon resonance sensors at the gold–water interface, *Sensor. Actuator. B Chem.* 134 (2) (2008) 854–862.
- [43] R.T. Beach, R.W. Christy, Electron-electron scattering in the intraband optical conductivity of Cu, Ag, and Au, *Phys. Rev. B* 16 (12) (1977) 5277–5284.
- [44] P.F. Maldague, C.A. Kukkonen, Electron-electron scattering and the electrical resistivity of metals, *Phys. Rev. B* 19 (12) (1979) 6172–6185.
- [45] B. Ben Doudou, H. Jaouadi, C. Dridi, Prism coupling technique investigation of optical and thermo-optical properties of polyvinyl alcohol and polyvinyl alcohol/silica nanocomposite films, *Opt Commun.* 492 (2021) 126984.
- [46] D. Viegas, M. Hernaéz, J. Goicoechea, et al., Simultaneous measurement of humidity and temperature based on an SiO₂-nanospheres film deposited on a long-period grating in-line with a fiber Bragg grating, *IEEE Sensor. J.* 11 (1) (2011) 162–166.
- [47] R. Mendis, D.M. Mittleman, Comparison of the lowest-order transverse-electric (TE₁) and transverse-magnetic (TM) modes of the parallel-plate waveguide for terahertz pulse applications, *Opt Express* 17 (17) (2009) 14839–14850.
- [48] H.S. Kim, S.H. Cha, B. Roy, et al., Humidity sensing using THz metamaterial with silk protein fibroin, *Opt Express* 26 (26) (2018) 33575–33581.
- [49] T.C. Tan, Y.K. Srivastava, R.T. Aho, et al., Active control of nanodielectric-induced THz quasi-BIC in flexible metasurfaces: a platform for modulation and sensing, *Adv. Mater.* 33 (27) (2021) 2100836.
- [50] D. Li, S. Lin, F. Hu, et al., Metamaterial terahertz sensor for measuring thermal-induced denaturation temperature of insulin, *IEEE Sensor. J.* 20 (4) (2020) 1821–1828.
- [51] A. Wexler, S. Hasegawa, Relative humidity-temperature relationships of some saturated salt solutions in the temperature range 0 degree to 50 degrees C, *Journal of research of the National Bureau of Standards* 53 (1954) 19–26.
- [52] C. He, S. Korposh, R. Correia, et al., Optical fibre sensor for simultaneous temperature and relative humidity measurement: towards absolute humidity evaluation, *Sensor. Actuator. B Chem.* 344 (2021) 130154.

- [53] Y. Ma, Y. Alattar, J. Zhou, et al., Semiconductor-based plasmonic interferometers for ultrasensitive sensing in a terahertz regime, *Opt Lett.* 42 (12) (2017) 2338–2341.
- [54] J. Xu, D. Liao, M. Gupta, Y. Zhu, S. Zhuang, R. Singh, L. Chen, Terahertz microfluidic sensing with dual-torus toroidal metasurfaces, *Adv. Opt. Mater.* 9 (2021) 2100024.
- [55] L. Chen, D. Liao, X. Guo, J. Zhao, Y. Zhu, S. Zhuang, Terahertz time-domain spectroscopy and micro-cavity components for probing samples: a review, *Frontiers of Information Technology & Electronic Engineering* 20 (5) (2019) 591–607.